

Deciphering satellite observations of compressional ULF waveguide modes

T. Elsdén,¹ A. N. Wright,¹ M. D. Hartinger,²

Abstract. We present an analytical method for determining incident and reflection coefficients for flank ULF compressional waveguide modes in Earth's magnetosphere. In the flank magnetosphere, compressional waves propagate azimuthally, but exhibit a mixed standing/propagating nature radially. Understanding this radial dependence will yield information on the energy absorption and transport of these waves. We provide a step by step method that can be applied to observations of flank ULF waves, which separates these fluctuations into incident and reflected parts. As a means of testing, we apply the method to data from a numerical waveguide simulation, which shows the effect on the reflection coefficient when energy is absorbed at a field line resonance.

1. Introduction

Ultra-Low frequency (ULF) waves have provided the foundation for a theoretical understanding of the dynamics of the magnetosphere since they were first discussed by *Dungey* [1954,1967]. Subsequently investigations into the theory of these waves considered the concept of wave coupling between fast and Alfvénic magnetohydrodynamic (MHD) waves in a cold, ideal plasma [*Southwood*, 1974; *Chen and Hasegawa*, 1974]. These works highlighted that the set of field lines on each L-shell had its own natural Alfvén frequency. Furthermore, *Southwood* [1974] examined the singularity occurring at the location where the fast mode frequency matched the Alfvén frequency, thus developing the concept of field line resonance (FLR). This process describes the transfer of energy from the fast to Alfvénic mode. While *Southwood* [1974] considered a Cartesian box geometry as a model of the dayside magnetosphere, *Chen and Hasegawa* [1974] discussed the same problem in a dipolar geometry to similar effect.

These studies were followed by *Kivelson and Southwood* [1985, 1986], also using the hydromagnetic box model, where the magnetosphere is treated as a closed cavity. These papers discussed how the large scale eigenmodes of this magnetospheric cavity could couple to FLRs, which provided an explanation for the observation of selected frequencies being excited by a broadband source. Such eigenmodes are termed global modes and are a standard feature of magnetospheric ULF wave modeling. At the same time, the field of numerical simulations developed rapidly, with many models addressing the problem of FLRs and cavity modes [e.g. *Allan et al.*, 1986a,1986b; *Zhu and Kivelson*, 1989; *Lee and Lysak*, 1989]. The present study however, is most closely linked to the waveguide model of *Rickard and Wright*, [1994] which expanded on the ideas presented by *Harrold and Samson*, [1992] and *Samson et al.*, [1992]. These works treat the magnetosphere as an open ended waveguide as opposed to a closed cavity. This allows for a continuum of wavenumbers in azimuth (k_y) and hence a continuum of waveguide

frequencies. The authors present further evidence and explanations for the coupling of fast and Alfvénic modes in the terrestrial magnetosphere within the context of a waveguide. The magnetosphere has also been shown to behave as a waveguide in global MHD simulations [*Claudepierre et al.*, 2015], giving further support to its use here.

The above concepts and references regarding ULF waves are introduced as they underpin the theory of this work. We present analytical and numerical models to study ULF waveguide modes in the flank magnetosphere. Our aim is to demonstrate a procedure that can subsequently be used in conjunction with observations. Compressional waveguide modes propagate azimuthally on the flanks but have a mixed standing/propagating nature in the radial direction. We decompose these fluctuations into radially propagating inward (incident) and outward (reflected) waves, which can provide information on energy transport and absorption in the flank magnetosphere. The analysis requires signals whose amplitudes do not vary drastically over one or two periods, and that have a well defined frequency. Space based observations of such ULF waves have been reported by *Rae et al.*, [2005], *Eriksson et al.*, [2006], *Clausen et al.*, [2008], *Hartinger et al.*, [2011] and *Hartinger et al.* [2012]. We apply our method of deriving these coefficients to simulated data, as a means of validating the procedure, with the aim of applications to real data in the future.

While methods exist for the routine identification and characterization of cavity modes in satellite observations [e.g., *Waters et al.*, 2002], there are no comparable techniques for waveguide modes. This adds uncertainty to waveguide/global mode observational studies. For example, in a statistical study estimating global mode occurrence rates outside the plasmasphere, *Hartinger et al.*, [2013] identified potential global modes using cavity mode selection criteria: globally coherent, monochromatic fast mode waves with electric/magnetic perturbations consistent with radially standing waves. As discussed by *Hartinger et al.*, [2013], these criteria excluded tailward propagating waveguide modes, likely biasing noon occurrence rates higher than flank rates and leading to an unrealistically low overall global mode occurrence rate.

The paper is organised as follows: Section 2 outlines the model geometry and the equations for the problem, then discusses the steps to follow to perform the analytic method used for deriving the incident and reflection coefficients. Section 3 discusses the application of our analytical model to simulated data. Here the numerical method and signal processing techniques employed are mentioned in detail. Concluding remarks are given in Section 4 and a full derivation of the procedure and reference equations are provided in Appendix A.

¹Mathematical Institute, University of St. Andrews, St. Andrews, Fife KY16 9SS, UK.

²Bradley Department of Electrical and Computer Engineering, Virginia Polytechnic Institute and State University, 1185 Perry St Rm 302, Blacksburg, Virginia, 24061 USA

2. Theory and Model

2.1. Waveguide Geometry

The Cartesian hydromagnetic box model has been extensively used to study the behaviour of ULF wave modes in the flank magnetosphere [e.g. *Southwood*, 1974; *Kivelson and Southwood* 1985, 1986]. $\hat{\mathbf{x}}$ is taken as the radial direction, positive outward. $\hat{\mathbf{y}}$ represents the azimuthal direction, with the antisunward direction being aligned with positive/negative $\hat{\mathbf{y}}$ on the dusk/dawn flank, respectively. $\hat{\mathbf{z}}$ is in the direction of the background magnetic field taken as $\mathbf{B} = B_0\hat{\mathbf{z}}$. Figure 1 gives a representation of this waveguide.

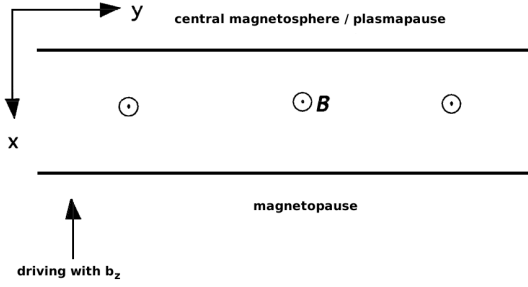


Figure 1. A schematic of the model magnetospheric waveguide. The magnetopause boundary is driven as indicated, launching waves propagating in y (azimuthally).

The plasma is assumed to be cold (low β) and ideal. The waveguide has a perfectly reflecting inner boundary in x modeling some natural boundary in space such as the plasmapause or a turning point, whilst the outer boundary (magnetopause) is driven. We consider only fundamental standing modes in the z direction, where field lines are fixed at their ionospheric footpoints by assuming nodes of velocity there. This reduces the computational model to a two dimensional waveguide allowing for faster computation and better resolution. The magnetic equator is placed at $z = 0$, and the single Fourier mode in z is expressed for each of the components as: $u_x, u_y, b_z \sim \cos(k_z z)$; $b_x, b_y \sim \sin(k_z z)$. This assumption is used in the component definitions given in Section 2.2. The inhomogeneity of the plasma is characterised by allowing the density to vary with radius (x). In the numerical simulations we normalise the equations to deal with dimensionless quantities, but for the analytical method we use the dimensional linearized MHD equations which can be expressed as

$$\frac{\partial b_x}{\partial t} = B_0 \frac{\partial u_x}{\partial z}, \quad (1)$$

$$\frac{\partial b_y}{\partial t} = B_0 \frac{\partial u_y}{\partial z}, \quad (2)$$

$$\frac{\partial b_z}{\partial t} = -B_0 \left(\frac{\partial u_x}{\partial x} + \frac{\partial u_y}{\partial y} \right), \quad (3)$$

$$\frac{\partial u_x}{\partial t} = \frac{V_A^2}{B_0} \left(\frac{\partial b_x}{\partial z} - \frac{\partial b_z}{\partial x} \right), \quad (4)$$

$$\frac{\partial u_y}{\partial t} = \frac{V_A^2}{B_0} \left(\frac{\partial b_y}{\partial z} - \frac{\partial b_z}{\partial y} \right), \quad (5)$$

where V_A is the Alfvén speed and B_0 the background magnetic field strength. For the analytic work in this paper, we assume the lowest order WKB approximation to the above equations (1)-(5). Analysis of this type is discussed in

detail in, for example, *Inhester*, [1987] and *Wright*, [1994]. This gives the radial wavenumber k_x as

$$k_x^2(x) = \frac{\omega^2}{V_A^2(x)} - k_y^2 - k_z^2, \quad (6)$$

with the phase in x defined as

$$\Phi_x(x) = \int^x k_x(x') dx'. \quad (7)$$

2.2. Tailward Traveling Wave Model

As mentioned previously, the goal of this study is to understand the dynamics of tailward traveling waves that exhibit a mixed propagating and standing nature radially. In this regard consider a wave of the form

$$b_x = A_i \cos(k_y y - \Phi_x - \omega t) \sin(k_z z) + A_r \cos(k_y y + \Phi_x - \omega t) \sin(k_z z). \quad (8)$$

A_i denotes the incident coefficient, A_r the reflected, both with units of Tesla. This stems from inward propagation being in the negative $\hat{\mathbf{x}}$ direction. k_x, k_y and k_z are the wavenumbers; x, y and z the positions in the $\hat{\mathbf{x}}, \hat{\mathbf{y}}$ and $\hat{\mathbf{z}}$ directions respectively. We choose to define the b_x component purely as a start point from which to derive the other component forms. Using equations (1)-(5) yields

$$b_y = -A_i \frac{k_y}{k_x} \cos(k_y y - \Phi_x - \omega t) \sin(k_z z) + A_r \frac{k_y}{k_x} \cos(k_y y + \Phi_x - \omega t) \sin(k_z z). \quad (9)$$

$$b_z = -\frac{A_i k_z}{k_x} \left\{ 1 - \frac{\omega^2}{V_A^2 k_z^2} \right\} \sin(k_y y - \Phi_x - \omega t) \cos(k_z z) + \frac{A_r k_z}{k_x} \left\{ 1 - \frac{\omega^2}{V_A^2 k_z^2} \right\} \sin(k_y y + \Phi_x - \omega t) \cos(k_z z). \quad (10)$$

$$u_x = -\frac{A_i}{B_0} \frac{\omega}{k_z} \sin(k_y y - \Phi_x - \omega t) \cos(k_z z) - \frac{A_r}{B_0} \frac{\omega}{k_z} \sin(k_y y + \Phi_x - \omega t) \cos(k_z z). \quad (11)$$

$$u_y = \frac{A_i}{B_0} \frac{\omega k_y}{k_x k_z} \sin(k_y y - \Phi_x - \omega t) \cos(k_z z) - \frac{A_r}{B_0} \frac{\omega k_y}{k_x k_z} \sin(k_y y + \Phi_x - \omega t) \cos(k_z z). \quad (12)$$

What is the problem we are trying to solve? The question is this: can we take the quantities given in satellite data and use them to determine the unknowns in the above system (8)-(12)? These unknowns are $A_i, A_r, k_x, k_y, k_z, \Phi_x$ and $k_z z$. The position in y is not required since the model assumes the wave is propagating in the $\hat{\mathbf{y}}$ direction. Hence changing y merely shifts the phase of the entire solution and is similar to moving the time origin, but does not affect any of the quantities listed above. Not all of the quantities provided from satellite data are independent, which reduces the number of ‘knowns’. These independent quantities are the amplitudes of b_x, b_y, b_z and u_x , the frequency ω , the local Alfvén speed V_A and the phase shift between b_x and b_y , denoted by ϕ . Stipulating $-\pi < \phi \leq \pi$, ϕ is positive if b_y leads b_x by less than π , and negative if b_y trails b_x by less than π . u_y is not an independent quantity as it can be expressed in terms of the amplitudes of u_x, b_x and b_y . Equally, any of these quantities could have been removed instead, in favor of u_y .

To proceed with determining the unknowns, it is useful to express the components in terms of a single amplitude and

phase for the purpose of comparison to data. For example, we express b_x as

$$b_x = \bar{b}_x \cos(\psi_1 - \omega t), \quad (13)$$

where \bar{b}_x is the amplitude and ψ_1 a phase shift. Considering this for all components, we can then equate the two expressions for each component e.g. (8) and (13). This allows the expression of the amplitudes in terms of the incident and reflection coefficients. After some algebra we derive the following system of equations:

$$\begin{aligned} \bar{b}_x &= \pm \sqrt{A_i^2 + A_r^2 + 2A_i A_r \cos(2\Phi_x) \sin(k_z z)}, \\ \bar{b}_y &= \pm \frac{k_y}{k_x} \sqrt{A_i^2 + A_r^2 - 2A_i A_r \cos(2\Phi_x) \sin(k_z z)}, \\ \bar{b}_z &= \pm \frac{k_z}{k_x} \left\{ \frac{\omega^2}{V_A^2 k_z^2} - 1 \right\} \sqrt{A_i^2 + A_r^2 - 2A_i A_r \cos(2\Phi_x) \cos(k_z z)}, \\ \bar{u}_x &= \pm \frac{\omega}{B_0 k_z} \sqrt{A_i^2 + A_r^2 + 2A_i A_r \cos(2\Phi_x) \cos(k_z z)}, \\ \tan(\phi) &= \frac{2A_i A_r \sin(2\Phi_x)}{A_r^2 - A_i^2}, \\ \frac{\omega^2}{V_A^2} &= k_x^2(x) + k_y^2 + k_z^2, \end{aligned}$$

where as mentioned above, \bar{b}_x , \bar{b}_y , \bar{b}_z and \bar{u}_x are the amplitudes of b_x , b_y , b_z and u_x respectively, and we restate the WKB fast mode dispersion relation from (6) as (19). This system contains six equations for the seven unknowns previously listed. It is therefore necessary to infer one more piece of information from the satellite data. Multiple satellite missions and ground-based observations have the capability of estimating one of the wavenumbers. For example, phase differences between signals measured at longitudinally spaced satellites or ground stations can be used to obtain k_y [e.g., *Mathie and Mann*, 2000; *Sarris et al.*, 2013] and phase differences between signals measured at multiple locations on the same field line can be used to obtain k_z [e.g., *Takahashi et al.*, 1987]. Once a component of the wavevector has been estimated, (14)-(19) may then be solved.

2.3. Solution Method

In this section we outline the steps to follow to determine the unknown quantities required to construct signals of the form of (8)-(12). The algebra for the full solution of equations (14)-(19) is given in Appendix A. The rearranging of the equations for the desired quantities differs depending on which of the wavenumbers is given from satellite measurements. Hence, we detail each case in the following sections 2.3.1, 2.3.2 and 2.3.3 in a step by step manner, referencing equations found in Appendix A. These sections discuss how to obtain the three wavenumbers which are then used in determining A_i and A_r , shown in section 2.3.4. Sections of the same name can be found in Appendix A detailing the full solution in each case.

2.3.1. k_z Measured

1. Use (A3) to find k_y , choosing the positive root for an observation in the dusk flank and the negative root for the dawn flank.

2. Use (A4) to find $k_x(x)$.

2.3.2. k_y Measured

1. Use (A5) to find k_z , taking the positive root.

2. Use (A4) to find $k_x(x)$.

2.3.3. k_x Measured

1. (A7) and (A8) together determine four values for k_y . Take the two positive values for a dusk flank observation and the two negative values for the dawn flank.

2. Use (A9) to find the corresponding k_z value.

2.3.4. Determining A_i and A_r

After completing steps 1 and 2 for one of the cases above, proceed to the steps below to determine A_i and A_r .

3. Use (A2) to find $k_z z$. Choose the positive sign for an observation above the magnetic equator ($z > 0$) and the negative sign for an observation below ($z < 0$).

(14) Given $k_z z$, determine the coefficients C and D from the first equalities in (A10) and (A11), and P and Q from (A19) and (A20) respectively.

5. Using P and Q in (A18) defines two values for A_i^2 , and hence four solutions for A_i .

6. (A21) yields two values of A_r for each A_i , giving eight solution pairs of A_i and A_r .

7. (A24) and (A25), with (A23), define four values of $\Phi(x)$ for each A_i and A_r combination, which implies a total of 32 solution combinations.

(15) Following the above systematic approach, all possible solutions can be determined. To eliminate the spurious solutions, the component time series are formed using equations (8)-(12) and are then compared to the data to see which ones match. It is this procedure which is followed in the next section.

3. Method Testing - Simulation Case Study

We now demonstrate how to test the above analytical method for determining incident and reflection coefficients on simulated data. This will establish the reliability of the method on numerical data before attempting to apply the method to satellite data. The following subsections outline the details of the simulation, how to generate appropriate signals to input to the method through signal analysis and the final results demonstrating the use of the method.

3.1. Numerical Model

Equations (1)-(5) are solved numerically using a leapfrog-trapezoidal algorithm [*Rickard and Wright*, 1994]. We first normalise the magnetic field by the background field strength B_0 , the density by that at the inner boundary $\rho(0)$ and the length by the width of the waveguide in x . Following *Wright and Rickard*, [1995b], we adopt a variation in the Alfvén speed of the form

$$V_A(x) = 1 - \frac{x}{x_0}, \quad 0 < x \leq x_c \quad (20)$$

$$V_A(x) = \frac{x_0 \left(1 - \frac{x_c}{x_0}\right)^3 (1 - x_c)}{(x_0 - 2x_c + 1)(1 - x_c) - (1 - x)^2}, \quad x_c < x < 1 \quad (21)$$

which is normalised to the Alfvén speed at $x = 0$. This profile is displayed in Figure 2. x_0 is used to adjust the gradient of the profile, therefore adjusting the width of the Alfvén continuum. x_c is the point where the linear profile smoothly transitions to a region of relatively uniform V_A . The linearity for $x \leq x_c$ produces a phase mixing length that is independent of radius, such that certain areas are not over or under resolved.

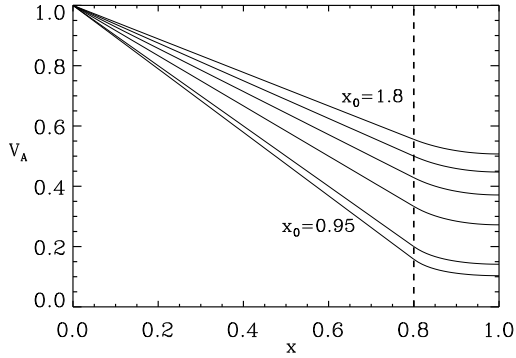


Figure 2. Variation of the Alfvén speed profile with radius (x) given by equations 20 and 21, adapted from *Wright and Rickard*, [1995b]. The plotted curves correspond to the values $x_0 = 0.95, 1.0, 1.2, 1.4, 1.6, 1.8$, with the first and last annotated. The dashed line represents the value of $x_c = 0.8$.

The waveguide has a radial extent of 1 which corresponds to a physical length of $10 R_E$. The length in y varies for the different simulations dependent on the wavelength. We choose an appropriate spatial resolution of the grid, timestep and total length of simulation to satisfy the Courant-Friedrichs-Lewy (CFL) condition and resolve the phase mixing length. Typically, energy is conserved to one part in 10^5 or better.

To model tailward traveling waves we drive the system with a running disturbance on the magnetopause, more details of which are given in the results section 3.3. The magnetopause boundary is driven by perturbations in the z component of the magnetic field, b_z . This has been demonstrated as an effective means of modeling driving by magnetic pressure [Elsden and Wright, 2015]. Furthermore, given a perfectly reflecting inner boundary, driving in this way allows the fundamental radial mode to be a quarter wavelength mode. This lowers the natural waveguide eigenfrequencies, bringing them more in line with the observed frequencies without resorting to an unphysical plasma density [Mann *et al.*, 1999].

To efficiently model an open-ended waveguide in y we introduce dissipation regions at either end (beyond the region of interest), which act to absorb any perturbations as if they had run out of the waveguide. This is implemented by adding a linear drag term to the equation of motion in these regions, the amplitude of which can be adjusted as per the strength of dissipation required.

3.2. Signal Generation and Analysis

Our procedure is appropriate for signals that are purely propagating in the y direction. The signal has to be relatively monochromatic and cannot display a great variation in amplitude over one period. To produce such a signal from our simulations we drive the outer boundary with a tailward traveling wave packet, an example of which will be given in section 3.3. Our control lies with the amplitude, wavelength, phase speed and number of cycles in the packet.

To model a satellite observation, we pick a location in the waveguide and consider the time series of the components. These signals are bandpass filtered using an IDL filtering routine, in a similar manner to the filtering of observational data. For our procedure we require the amplitudes of the components and the phase shift between b_x and b_y , as discussed in section 2.2. To derive these from the simulation data we use an analytic signal method over the desired time

interval, which has been used in observations by, for example, *Glassmeier et al.*, [1980]; *Hartinger et al.*, [2011]. The analytic signal $s_a(t)$ is a complex valued function formed from the real signal $s(t)$ and its Hilbert transform $\hat{s}(t)$ as

$$s_a(t) = s(t) + i\hat{s}(t). \quad (22)$$

This removes any negative frequency contributions to the signal. In this form the instantaneous phase of each signal, ψ , is determined by

$$\psi = \tan^{-1} \left(\frac{\hat{s}(t)}{s(t)} \right), \quad (23)$$

and hence we can calculate the required phase shift between the b_x and b_y components. The amplitude envelope for the signal is determined from

$$|s_a(t)| = \sqrt{s(t)^2 + \hat{s}(t)^2}, \quad (24)$$

which is averaged over the cycles considered to determine their amplitude. This then yields all the required information to determine the incident and reflection coefficients.

An interesting way to test the method is to absorb some of the energy at a field line resonance at a specific location in x . If we place a satellite on the magnetopause side of the resonance we should see an overall inward flow of energy as energy is converted from the compressional fast mode to Alfvénic oscillations. This should mean that the incident coefficient is considerably larger than the reflection coefficient if the wave coupling is efficient. The position of the resonance can be controlled by the driving frequency and the Alfvén speed profile. The resonance will be excited at the location where the fast mode frequency matches the local Alfvén frequency. Rather than driving the resonance with a natural waveguide eigenfrequency, we choose to drive the resonance with the boundary driving frequency, tuning the equilibrium such that a waveguide resonance is not excited, allowing for a clearer signal for the first testing of this method.

k_z is taken to be $\pi/2$ in dimensionless units (corresponding to a dimensional field line length of $20R_E$) and the parameter controlling the gradient of the Alfvén speed profile, x_0 , is set to 2.7, such that the FLR continuum does not overlap any of the $k_y = 0$ waveguide eigenfrequencies as mentioned above. The other parameter in the Alfvén speed definition ((20) and (21)), x_c , is chosen as 0.8. We choose to excite an Alfvén resonance in the guide at $x_r = 0.2$, by setting the driving frequency equal to the Alfvén frequency at this location. This yields a dimensionless angular driving frequency of $\omega_r = 1.4544$. k_y varies between each simulation and will control the efficiency of the coupling between the fast and Alfvénic modes. The modes are decoupled in the $k_y \rightarrow 0$ and $k_y \rightarrow \infty$ limits and hence we expect the strongest coupling for moderate k_y values [Kivelson and Southwood, 1986]. The maximum k_y is determined such that the mode is oscillatory (not evanescent) in x at the satellite location. The driving frequency is held constant between the different simulations by varying the phase speed of the driver accordingly.

Before stating the results, we list a step by step view of the method for clarity.

1. Specify a wavelength and phase speed for the magnetopause driver then run the simulation.
2. Choose the satellite location on the magnetopause side of the resonance, retrieve component time series.
3. Bandpass filter the data around the driving frequency.
4. Use the analytic signal method to determine instantaneous phase and amplitude.
5. Derive all possible solution combinations for A_i , A_r values, as per Section 2.3.

6. Select correct solutions by reconstructing the signal using A_i and A_r and comparing to the simulation signal.

3.3. Results

One of the simulation runs for a specific value of k_y will be discussed to demonstrate the method. For the equilibrium parameters described above the value of k_y can vary over $0 \leq k_y \leq 1.503$, the upper bound being determined by maintaining an oscillatory nature in x at the magnetopause. An example of the temporal and spatial dependence of the magnetopause driver is given in Figure 3, for the case $k_y = 1.4$. Note that the spatial form of the driving condition is a sine wave that travels in the y direction at a speed ω/k_y and is nonzero over the window $-5 < y < 5$ in this example. The frequency ω is chosen to match the Alfvén frequency at $x_r = 0.2$, hence these parameters determine the azimuthal phase speed of the magnetopause driver we impose.

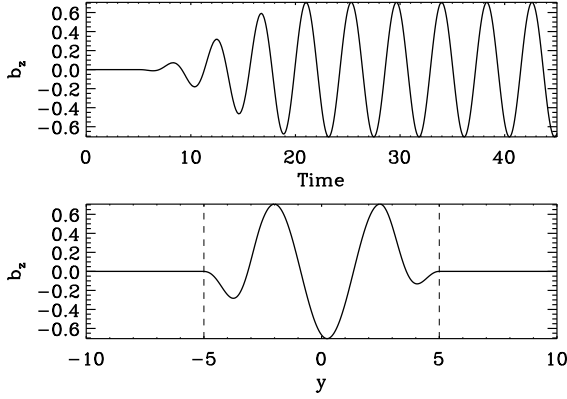


Figure 3. Top panel: temporal variation of the perturbation b_z on the driven magnetopause boundary ($x = 1$), in the center of the driven section. Bottom panel: spatial variation in azimuth of b_z on the driven magnetopause boundary, at time $t = 45$. The vertical dashed lines represent the start of the dissipation regions ($y < -5$, $y > 5$), where the boundary is not driven.

We select a location in the waveguide for the model satellite of $x = 0.9$, $y = 0$, $z = 0.5$. The position is chosen close to the magnetopause boundary such that the mode is oscillatory and not evanescent in x . The location $y = 0$ corresponds to the centre of the driven magnetopause section, not to the subsolar point as is typical in GSE/GSM coordinates. A time series plot over the course of the simulation at this location for each of the components of the magnetic field, velocity and Poynting vector, is displayed in Figure 4. The driving has produced the intended signals, of relatively constant amplitude and monochromatic nature. Panel 7 of the azimuthal Poynting vector S_y shows that the wave is purely tailward traveling as required for our analysis. The sixth panel displays a predominantly inward radial Poynting vector S_x , suggesting energy is being deposited in the waveguide interior. The monochromatic nature of the signal is confirmed by considering the FFT power spectra, displayed in Figure 5 for b_z at the satellite location. The an-

gular driving frequency of 1.4544 is reproduced as a cyclic

frequency of 0.23.

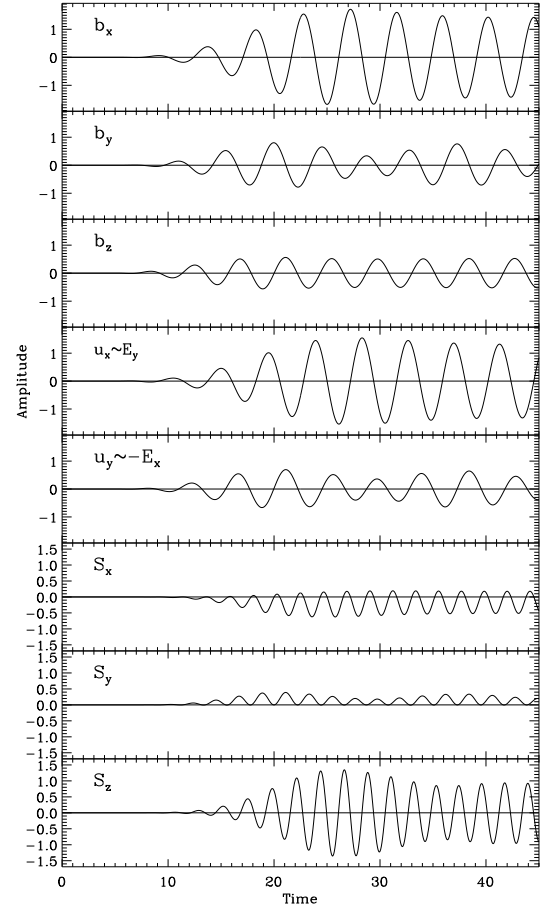


Figure 4. Component time series from satellite location $x = 0.9$, $y = 0$ and $z = 0.5$. Top three panels are the magnetic field components, panels four and five are the velocity components, panels six to eight are the Poynting vector components.

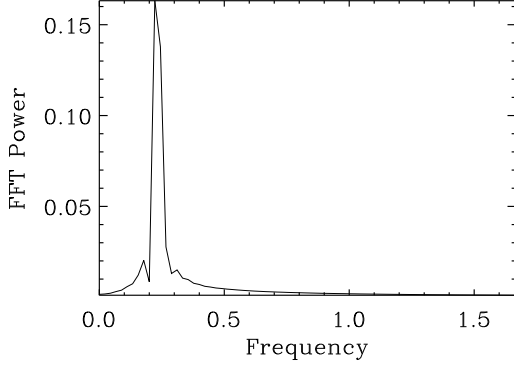


Figure 5. FFT power spectrum of the unfiltered b_z signal at location $x = 0.9$, $y = 0$ and $z = 0.5$, showing a dimensionless cyclic frequency of 0.23 corresponding to the driving frequency.

To check that a resonance is being excited at the appropriate location, we check the behaviour of the transverse magnetic field and velocity components. Figure 6 shows the secular growth in time of these components, which is expected for a steadily driven resonance in the absence of dissipation.

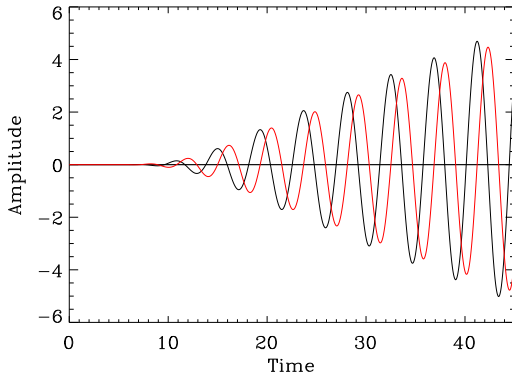


Figure 6. Time series of b_y (black) and u_y (red) at the Alfvén resonance location $x = 0.2$, with $y = 0$.

The next step is to bandpass filter the data for the desired frequency. Considering the idealized case that we present here, the effect of filtering is not drastic, but still is a worthwhile procedure to demonstrate how our method would be applied to a real data signal. A small time interval covering 1-2 periods is reconstructed from the signal filtered over

cyclic frequencies from 0.17 to 0.29. The top panel of Figure 7 displays the unfiltered and filtered signals.

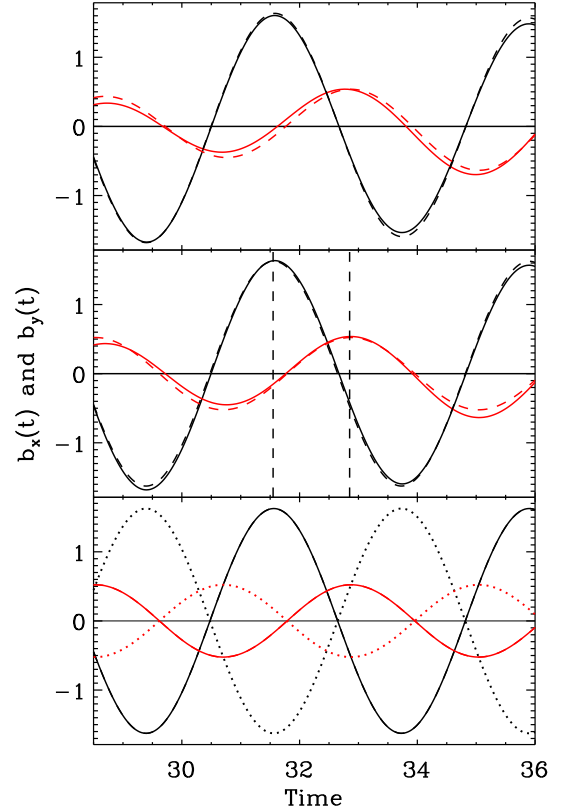


Figure 7. Time series interval from $t = 28.5$ to $t = 36.0$ of b_x (black) and b_y (red) showing: top panel - the unfiltered data (solid) with the bandpass filtered data (dashed); middle panel - filtered data (solid) with phase and amplitude averaged signal (dashed), vertical dashed lines indicate the phase shift ϕ ; bottom panel - phase and amplitude averaged data (solid), reconstructed signal from A_i and A_r values (dashed, which overlies the solid line exactly in this example). The dotted lines represent a spurious solution that does not reproduce the desired (solid line) signals, so is discarded.

Now that the time interval has been selected, the method of the analytic signal is employed to determine the instantaneous phase and average amplitude for each component time series. These quantities are required for determining the incident and reflection coefficients. We apply the method to the whole signal, then select the desired time interval. Subtracting the instantaneous phase of the b_y signal from the b_x signal, yields their relative phase difference, which is referred to as ϕ in the method outlined in sections 2.2 and 2.3. The average amplitudes are determined by averaging the signal envelope over the cycles selected. To test the analytic signal method, we fit sinusoids with the derived amplitudes and phases and plot against the bandpass filtered simulation signals. This is displayed as the middle panel of Figure 7. The vertical dashed lines indicate the value of $\phi = 109.15^\circ$, taken as the phase by which b_y leads b_x as this is less than 180° (see Section 2.2 for discussion on choosing ϕ). Since the filtered signal is already of near constant amplitude and frequency, the dashed line representing the signal constructed

from the instantaneous phase and average amplitude lies almost directly on top.

All of the knowns are now determined and the system can be solved as described in Section 2.3. This yields the incident and reflection coefficients A_i and A_r . For the simulation in question, the absolute value of these coefficients was determined as $|A_i| = 1.202$ and $|A_r| = 1.112$. These correct solutions are found by matching the signal components reconstructed from the derived quantities as per (8)-(12), with the phase and amplitude averaged signal. The bottom panel of Figure 7 displays these signals for the b_x (black) and b_y (red) components. The dotted lines represent a reconstructed solution that does not match the solid lines, so represents a spurious solution that we shall discard. The dashed lines are barely visible as they lie directly on top of the original signal, which confirms the values of A_i and A_r used to produce them correspond to the correct roots.

Furthermore, the correct values are in line with our original prediction, that the reflection coefficient will be smaller than the incident due to energy lost from the fast mode at the resonance. The amount of energy deposited and hence the ratio of the reflected to incident coefficients is dependent on the efficiency of the wave coupling, which is controlled by k_y . If k_y is small, the gradients of b_z in the \hat{y} direction which drive the resonance become small and hence the coupling is weak. For large k_y , the turning point of the mode retreats from the resonance toward the magnetopause boundary, and the amplitude decays evanescently, meaning the fast mode does not penetrate to the resonance location. This behaviour produces a classic curve of absorption against k_y (see Figure 2 *Kivelson and Southwood*, [1986]). As a test of the values produced for A_i and A_r , we ran several simulations for different values of k_y , performed the same analysis as above, and plotted the resulting ratio of A_r to A_i . This is displayed in Figure 8. A clear trend appears showing the ratio tending to one where little energy is transferred to the resonance (as in the $k_y = 1.4$ case above), while in regions where the coupling is more efficient, the ratio drops considerably. This is further confirmation that the method employed to determine the incident and reflection coefficients is behaving consistently.

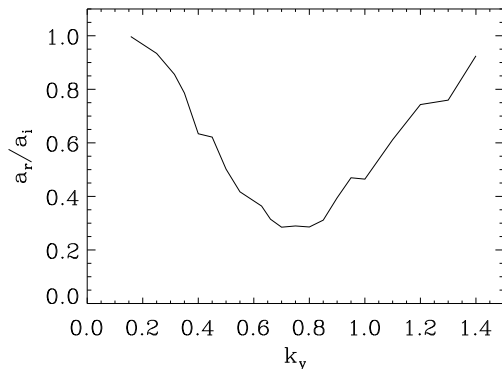


Figure 8. The ratio A_r/A_i plotted against k_y for twenty one different k_y values.

4. Conclusions

In this work we have introduced a method for determining incident and reflection coefficients for flank ULF waveguide modes. This method is valid for tailward traveling waves of roughly constant amplitude with a clearly defined frequency. Despite seeming like an idealized case, observations

of such signals have been recently published [*Rae et al.*, 2005; *Eriksson et al.*, 2006; *Clausen et al.*, 2008; *Hartinger et al.*, 2011,2012]. The coefficients derived are correlated with the energy absorption of the magnetospheric interior, as demonstrated by the lowering of the reflection coefficient when energy is absorbed at a FLR. The method produces consistent results, reproducing a similar resonant absorption curve to that of *Kivelson and Southwood*, [1986], showing the change in the efficiency of wave coupling with azimuthal wavenumber. Since the only requirements of the method are a set of time series together with certain amplitudes and phase shifts, this technique could also be applied to results from a global MHD simulation. Evidently, the Cartesian geometry used in our modelling is a simplification. Future studies could employ spatial eigenmodes based upon a realistic magnetospheric equilibrium and so improve the accuracy of our technique when applied to satellite data or results from global magnetospheric simulations. The overall purpose of this work has been to test the method on simulation data in preparation for using it with satellite observations of flank ULF compressional modes in the future.

Appendix A: Solution Method

We outline the solution method for solving the system of equations (14)-(19). From satellite data it is assumed that the amplitudes of b_x , b_y , b_z and u_x (denoted by \bar{b}_x , \bar{b}_y , \bar{b}_z and \bar{u}_x) are known. Further to this, we require the frequency ω , the Alfvén speed V_A and the phase difference between b_y and b_x , denoted by ϕ (refer to Section 2.3 for full details on ϕ). As discussed at the end of Section 2.2, one of the wavenumbers is also required to solve the system. In each of the sections below, we discuss the different approaches depending on which wavenumber is estimated most accurately. Firstly however, we must resolve the choices of signs in equations (14)-(19). Since it is the amplitudes of the components (denoted by an overscore) that are being used, the expressions for these amplitudes must be positive. Hence the choice of sign is dependent on the signs of $\sin(k_z z)$ and $\cos(k_z z)$. For a fundamental mode in the \hat{z} direction, $-\pi/2 < k_z z < \pi/2$. $\cos(k_z z)$ is positive over the range of $k_z z$, and hence the signs in equations (16) and (17) are taken to be positive. If the observation is taken below the magnetic equator, z is less than zero, which implies $\sin(k_z z) < 0$ and hence we choose negative signs for equations (14) and (15) such that the amplitudes remain positive. Equally if the satellite is above the magnetic equator, positive signs are taken in these equations.

There is one exception to this which occurs when k_y is negative, since k_y appears as a coefficient in (15). If the observation is in the dusk flank, take k_y to be positive, and if in the dawn flank, take k_y to be negative. This stems from the positive \hat{y} direction being tailward in the dusk flank. Therefore in the situation where k_y is negative, the above sign choices must be reversed for equation (15) such that the amplitude remains positive.

A1. k_z Measured

To begin with, consider the case where k_z , the field aligned wavenumber, is known from observations. To find the position z we divide (14) by (17) to give

$$\tan(k_z z) = \pm \frac{\omega \bar{b}_x}{k_z \bar{u}_x} \frac{1}{B_0}, \quad (\text{A1})$$

$$\Rightarrow k_z z = \tan^{-1} \left(\pm \frac{\omega \bar{b}_x}{k_z \bar{u}_x} \frac{1}{B_0} \right), \quad (\text{A2})$$

where the sign choice is determined from the position in z above or below the magnetic equator (positive if $z > 0$). k_y can be determined from the ratio of (16) to (15), substituting for $\tan(k_z z)$ using (A1) to give

$$\begin{aligned} \frac{\bar{b}_z}{\bar{b}_y} &= \pm \frac{B_0}{\omega k_y} \left(\frac{\omega^2}{V_A^2} - k_z^2 \right) \frac{\bar{u}_x}{\bar{b}_x}, \\ \Rightarrow k_y &= \pm \frac{\bar{u}_x \bar{b}_y}{\bar{b}_x \bar{b}_z} \frac{B_0}{\omega} \left(\frac{\omega^2}{V_A^2} - k_z^2 \right), \end{aligned} \quad (\text{A3})$$

where the plus/minus root is taken for observations on the dusk/dawn flank. $k_x(x)$ can now be determined from the fast mode dispersion relation (6) as

$$k_x(x) = \sqrt{\frac{\omega^2}{V_A^2} - k_y^2 - k_z^2}, \quad (\text{A4})$$

where $k_x(x)$ is taken to be positive (inward and outward propagation in x is accommodated in the definition of b_x in equation (8)). At this point, $k_z z$, k_y and $k_x(x)$ are known and we can proceed to section A4 to calculate A_i and A_r .

A2. k_y Measured

If instead k_y , the azimuthal wavenumber, is provided by satellite data we proceed in a similar manner to the above for k_z . Rearranging (A3) gives

$$k_z = \sqrt{\frac{\omega^2}{V_A^2} - |k_y| \frac{\omega}{B_0} \frac{\bar{b}_x \bar{b}_z}{\bar{u}_x \bar{b}_y}}. \quad (\text{A5})$$

The absolute value sign here covers the cases for $k_y > 0$ and $k_y < 0$, which both result in the same expression for k_z . The positive root is taken for k_z since the sign of $k_z z$ is determined by the choice of z either above or below the magnetic equator. The value of $k_z z$ is then determined from A2. Now given k_y and k_z , $k_x(x)$ is determined from (A4) as previously, and we can again proceed to section A4 to find A_i and A_r .

A3. k_x Measured

The case where k_x , the radial wavenumber, is provided from observations is not so straightforward as we lack an expression for one of the other wavenumbers in terms of k_x alone. We proceed by rewriting (A3) using (A4) as

$$k_y = \pm \frac{\bar{u}_x \bar{b}_y}{\bar{b}_x \bar{b}_z} \frac{B_0}{\omega} (k_x^2(x) + k_y^2). \quad (\text{A6})$$

Again the sign for k_y is determined as being positive on the dusk flank and negative on the dawn flank. Rearranging (A6) as a quadratic for k_y and solving yields

$$k_y = \pm \frac{X}{2} \pm \sqrt{\frac{X^2}{4} - k_x(x)^2}, \quad (\text{A7})$$

where

$$X = \frac{\bar{b}_x \bar{b}_z}{\bar{u}_x \bar{b}_y} \frac{\omega}{B_0}. \quad (\text{A8})$$

For $k_y > 0$ choose the first sign to be positive, while for $k_y < 0$ choose the first sign to be negative. The second sign choice represents two distinct solutions which have to

be carried through the procedure until they can be tested for their validity. This doubles the total number of possible solutions, and indeed each of the above k_y values can lead to a correct solution. For this reason, it is preferable for the azimuthal or field aligned wavenumbers to be provided instead of the radial wavenumber, as for these cases a single solution can always be determined. Once the values of k_y have been calculated, the corresponding k_z values are determined from the fast mode dispersion relation as

$$k_z = \sqrt{\frac{\omega^2}{V_A^2} - k_y^2 - k_x^2(x)}, \quad (\text{A9})$$

and then the values of $k_z z$ are found from (A2). Now that the wavenumbers are known, proceed to section A4.

A4. Determining A_i and A_r

The above steps outline how to determine the wavenumbers depending on which is provided by the observation. The following working shows how then to calculate the incident and reflection coefficients A_i and A_r given the wavenumbers. We begin by squaring (14) and (15), then adding and subtracting to give

$$C = \bar{b}_x^2 + \frac{k_x^2}{k_y^2} \bar{b}_y^2 = 2(A_i^2 + A_r^2) \sin^2(k_z z), \quad (\text{A10})$$

$$D = \bar{b}_x^2 - \frac{k_x^2}{k_y^2} \bar{b}_y^2 = 4A_i A_r \cos(2\Phi_x) \sin^2(k_z z). \quad (\text{A11})$$

We attempt to form the terms on the right hand side of (18). The denominator can be written using (A10), as

$$A_r^2 - A_i^2 = A_r^2 + A_i^2 - 2A_i^2 = \frac{C}{2\sin^2(k_z z)} - 2A_i^2. \quad (\text{A12})$$

The numerator can be formed using (A11) as

$$2A_i A_r \sin(2\Phi_x) = \pm \frac{1}{2} \sqrt{16A_i^2 A_r^2 - \frac{D^2}{\sin^4(k_z z)}}. \quad (\text{A13})$$

Using (A12) and (A13) in (18) gives

$$\begin{aligned} \tan(\phi) &= \frac{\pm \frac{1}{2} \sqrt{16A_i^2 A_r^2 - \frac{D^2}{\sin^4(k_z z)}}}{\frac{C}{2\sin^2(k_z z)} - 2A_i^2} \\ \Rightarrow \tan^2(\phi) \left(\frac{C}{2\sin^2(k_z z)} - 2A_i^2 \right)^2 &= \frac{1}{4} \left(16A_i^2 A_r^2 - \frac{D^2}{\sin^4(k_z z)} \right). \end{aligned} \quad (\text{A14})$$

The goal is to eliminate A_r in terms of A_i . Expanding brackets and replacing A_r^2 using a rearrangement of (A12), we arrive at a fourth order equation for A_i as

$$A_i^4 - \frac{C}{2\sin^2(k_z z)} A_i^2 + \frac{C^2 \sin^2 \phi + D^2 \cos^2 \phi}{16\sin^4(k_z z)} = 0. \quad (\text{A16})$$

The above equation can be written as

$$A_i^4 - P A_i^2 + Q = 0, \quad (\text{A17})$$

$$\Rightarrow A_i^2 = \frac{P}{2} \pm \frac{1}{2} \sqrt{P^2 - 4Q}, \quad (\text{A18})$$

where

$$P = \frac{C}{2 \sin^2(k_z z)}, \quad (\text{A19})$$

$$Q = \frac{C^2 \sin^2 \phi + D^2 \cos^2 \phi}{16 \sin^4(k_z z)}. \quad (\text{A20})$$

(A18) defines four solutions for A_i given C , D , P and Q . Through squaring, spurious roots will have been introduced that will be discarded at the end. A_r is found from rearranging (A12) as

$$A_r = \pm \sqrt{P - A_i^2}. \quad (\text{A21})$$

This implies that there are eight possible combinations of A_i and A_r values. Each of these combinations can then be used to calculate the WKB phase Φ_x . Rearranging (14) gives

$$2A_i A_r \cos(2\Phi_x) = \frac{\bar{b}_x^2}{\sin^2(k_z z)} - A_i^2 - A_r^2, \quad (\text{A22})$$

$$\Phi_x = \frac{1}{2} \cos^{-1} \left\{ \frac{1}{2A_i A_r} \left(\frac{\bar{b}_x^2}{\sin^2(k_z z)} - A_i^2 - A_r^2 \right) \right\}.$$

Taking the inverse cosine results in four solutions for Φ_x , which can be expressed as

$$\Phi_x = \frac{1}{2} \cos^{-1}(\alpha) + n\pi, \quad n = 0, 1, \quad (\text{A24})$$

$$\Phi_x = \frac{1}{2} (2\pi - \cos^{-1}(\alpha)) + n\pi, \quad n = 0, 1, \quad (\text{A25})$$

where α is the curly bracketed term in (A23), and \cos^{-1} lies between 0 and π . Thus with four solutions for $\Phi_x(x)$ and eight combinations of A_i and A_r , there are 32 possible solutions. The correct solutions are determined by constructing the components given in (8)-(12) using the derived values of A_i , A_r etc, then checking these signals against the data. The solutions associated with the spurious roots acquired during the calculation may be identified and disregarded as the reconstructed signals will not match the original ones. This procedure will leave four valid combinations, one for each of the arbitrary phase choices in (A24) and (A25). Any one of these solutions may be used unless additional information is available to identify a particular solution as being more appropriate.

Acknowledgments. T. Elsdén would like to thank STFC for financial support for a doctoral training grant, number AMC3 STFC12. A. N. Wright was supported by STFC grant ST/N000609/1. Data from simulation results are available on request from T. Elsdén, email: te55@st-andrews.ac.uk.

References

- Allan, W., E. M. Poulter, and S. P. White (1986a), Impulse-excited hydromagnetic cavity and field-line resonances in the magnetosphere, *Planet. Space Sci.*, *34*(4), 371-385, doi:10.1016/0032-0633(86)90144-3
- Allan, W., E. M. Poulter, and S. P. White (1986b), Hydromagnetic wave coupling in the magnetosphere Plasmopause effects on impulse-excited resonances, *Planet. Space Sci.*, *34*(12), 1189-1200, doi:10.1016/0032-0633(86)90056-5
- Chen, L., and A. Hasegawa (1974), A theory of long-period magnetic pulsations: 1. Steady state excitation of field line resonance, *J. Geophys. Res.*, *79*(7), 1024-1032, doi:10.1029/JA079i007p01024.

- Claudepierre, S. G., F. R. Toffoletto, and M. Wiltberger (2015), Global MHD modeling of resonant ULF waves: Simulations with and without a plasmasphere, *J. Geophys. Res. Space Physics*, *120*, doi:10.1002/2015JA022048.
- Clausen, L. B. N., Yeoman, T. K., Behlke, R., and Lucek, E. A. (2008), Multi-instrument observations of a large scale Pc4 pulsation, *Ann. Geophys.*, *26*, 185-199, doi:10.5194/angeo-26-185-2008.
- Dungey, J.W. (1954), Electrodynamics of the outer atmosphere, Pennsylvania State, University Ionos. Res. Lab. Sci. Rept. No. 69.
- Dungey, J.W. (1967), Hydromagnetic waves, in *Physics of Geomagnetic Phenomena*, edited by S. Matsushita and W.H. Campbell, vol. 2, Academic, San Diego, Calif., pp. 913-934.
- Elsden, T., Wright, A. N. (2015), The use of the Poynting vector in interpreting ULF waves in magnetospheric waveguides, *J. Geophys. Res. Space Physics*, *120*, 166-186, doi:10.1002/2014JA020748.
- Eriksson, P.T.I., L.G. Bloomberg, S. Schaefer, and K.-H. Glassmeier (2006), On the excitation of ULF waves by solar wind pressure enhancements, *Ann. Geophys.*, *24*, 3161-3172, doi:10.5194/angeo-24-3161-2006.
- Glassmeier, K. H. (1980), Magnetometer array observations of a giant pulsation event, *J. Geophys.*, *48*(3), 127-138.
- Harrold, B. G., and J. C. Samson (1992), Standing ULF modes of the magnetosphere: A theory, *Geophys. Res. Lett.*, *19*, 1811, doi:10.1029/92GL01802.
- Hartinger, M., V. Angelopoulos, M. B. Moldwin, K.-H. Glassmeier, and Y. Nishimura (2011), Global energy transfer during a magnetospheric field line resonance, *Geophys. Res. Lett.*, *38*, L12101, doi:10.1029/2011GL047846.
- Hartinger, M., V. Angelopoulos, M. B. Moldwin, Y. Nishimura, D. L. Turner, K.-H. Glassmeier, M. G. Kivelson, J. Matzka, and C. Stolle (2012), Observations of a Pc5 global (cavity/waveguide) mode outside the plasmasphere by THEMIS, *J. Geophys. Res.*, *117*, A06202, doi:10.1029/2011JA017266.
- Hartinger, M. D., V. Angelopoulos, M. B. Moldwin, K. Takahashi, and L. B. N. Clausen (2013), Statistical study of global modes outside the plasmasphere, *J. Geophys. Res. Space Physics*, *118*, 804822, doi:10.1002/jgra.50140.
- Inhester, B. (1987), Numerical modeling of hydromagnetic wave coupling in the magnetosphere, *J. Geophys. Res.*, *92*(A5), 4751-4756, doi:10.1029/JA092iA05p04751.
- Kivelson, M. G., and D. J. Southwood (1985), Resonant ULF waves: A new interpretation, *Geophys. Res. Lett.*, *12*(1), 49-52, doi:10.1029/GL012i001p00049.
- Kivelson, M. G., and D. J. Southwood (1986), Coupling of global magnetospheric MHD eigenmodes to field line resonances, *J. Geophys. Res.*, *91*(A4), 4345-4351, doi:10.1029/JA091iA04p04345.
- Lee, D. H., and R. L. Lysak (1989), Magnetospheric ULF wave coupling in the dipole model: The impulsive excitation, *J. Geophys. Res.*, *94*(A12), 17097-17103, doi:10.1029/JA094iA12p17097.
- Mann, I. R., A. N. Wright, K. J. Mills, and V. M. Nakariakov (1999), Excitation of magnetospheric waveguide modes by magnetosheath flows, *J. Geophys. Res.*, *104*(A1), 333-353, doi:10.1029/1998JA900026.
- Mathie, R.A. and I.R. Mann (2000), Observations of Pc5 field line resonance azimuthal phase speeds: A diagnostic of their excitation mechanism, *J. Geophys. Res. Space Physics*, *105*, 10713-10728, doi:10.1029/1999JA000174.
- Rae, I.J., E.F. Donovan, I.R. Mann, F.R. Fenrich, C.E.J. Watt, D.K. Milling, M. Lester, B. Lavraud, J.A. Wild, H.J. Singer, H. Reme, and A. Balogh (2005), Evolution and characteristics of global Pc5 ULF waves during a high speed solar wind speed interval, *J. Geophys. Res. Space Physics*, *110*, A12211, doi:10.1029/2005JA011007.
- Rickard, G. J., and A. N. Wright (1994), Alfvén resonance excitation and fast wave propagation in magnetospheric waveguides, *J. Geophys. Res.*, *99*(A7), 13455-13464, doi:10.1029/94JA00674.
- Samson, J.C., B.G. Harrold, J.M. Ruohoniemi and A.D.M. Walker (1992), Field line resonances associated with MHD waveguides in the magnetosphere, *Geophys. Res. Lett.*, *19*, 441, doi:10.1029/92GL00116.

- Sarris, T. E., X. Li, W. Liu, E. Argyriadis, A. Boudouridis, and R. Ergun (2013), Mode number calculations of ULF field-line resonances using ground magnetometers and THEMIS measurements, *J. Geophys. Res. Space Physics*, *118*, 69866997, doi:10.1002/2012JA018307.
- Southwood, D. J. (1974), Some features of field line resonances in the magnetosphere, *Planete. Space Sci.*, *22*(3), 483-491, doi:10.1016/0032-0633(74)90078-6.
- Takahashi, K., J.F. Fennell, E. Amata, and P.R. Higbee (1987), Field-aligned structure of the Storm Time Pc 5 Wave of November 14-15, 1979, *J. Geophys. Res. Space Physics*, *92*, 5857-5864, doi:10.1029/JA092iA06p05857.
- Waters, C. L., K. Takahashi, D.-H. Lee, and B. J. Anderson (2002), Detection of ultralow-frequency cavity modes using spacecraft data, *J. Geophys. Res.*, *107*(A10), 1284, doi:10.1029/2001JA000224.
- Wright, A. N. (1994), Dispersion and wave coupling in inhomogeneous MHD waveguides, *J. Geophys. Res.*, *99*(A1), 159-167, doi:10.1029/93JA02206.
- Wright, A. N., and G. J. Rickard (1995a), A numerical study of resonant absorption in a magnetohydrodynamic cavity driven by a broadband spectrum, *Astrophys. J.*, *444*, 458-470, doi:10.1086/175620.
- Wright, A. N., and G. J. Rickard (1995b), ULF pulsations driven by magnetopause motions: Azimuthal phase characteristics, *J. Geophys. Res.*, *100*(A12), 23703-23710, doi:10.1029/95JA01765.
- Zhu, X., and M. G. Kivelson (1989), Global mode ULF pulsations in a magnetosphere with a nonmonotonic Alfvén velocity profile, *J. Geophys. Res.*, *94*(A2), 1479-1485, doi:10.1029/JA094iA02p01479.
-